IOPscience iopscience.iop.org

Home Search Collections Journals About Contact us My IOPscience

The carrier blocking effect on 850 nm InAlGaAs/AlGaAs vertical-cavity surface-emitting lasers

This content has been downloaded from IOPscience. Please scroll down to see the full text.

2006 Semicond. Sci. Technol. 21 1488

(http://iopscience.iop.org/0268-1242/21/10/023)

View the table of contents for this issue, or go to the journal homepage for more

Download details:

IP Address: 140.113.38.11
This content was downloaded on 26/04/2014 at 08:41

Please note that terms and conditions apply.

Semicond. Sci. Technol. **21** (2006) 1488–1494 doi:10.1088/0268-1242/21/10/023

The carrier blocking effect on 850 nm InAlGaAs/AlGaAs vertical-cavity surface-emitting lasers

Yi-An Chang[1], Tsung-Shine Ko[1], Jun-Rong Chen[1,2], Fang-I Lai[3], Chun-Lung Yu[3], I-Tsung Wu[3], Hao-Chung Kuo[1], Yen-Kuang Kuo[2], Li-Wen Laih[4], Li-Horng Laih[4], Tin-Chang Lu[1] and Shing-Chung Wang[1]

[1] Department of Photonics & Institute of Electro-Optical Engineering, National Chiao-Tung University, Hsinchu, 300, Taiwan
[2] Department of Physics, National Changhua University of Education, Changhua, 500, Taiwan
[3] Department of Electrical Engineering, Ching Yung University, Jung-Li, 320, Taiwan
[4] Millennium Communication Co., Hsinchu Industrial Park, 303, Taiwan

E-mail: hckuo@faculty.nctu.edu.tw

Received 18 June 2006, in final form 28 July 2006
Published 11 September 2006
Online at stacks.iop.org/SST/21/1488

Abstract
In this study, the carrier blocking effect on 850 nm InAlGaAs/AlGaAs vertical-cavity surface-emitting layers (VCSELs) was theoretically and experimentally investigated. By means of inserting a high-bandgap electron blocking layer, which was either 10 nm thick $Al_{0.75}Ga_{0.25}As$ or 13 nm thick $Al_{0.9}Ga_{0.1}As$, on the p-side of a quantum-well active region, the laser output performance was theoretically found to be improved. VCSELs with and without an electron blocking layer were also experimentally demonstrated. It was found that the threshold current was reduced from 1.47 to 1.33 mA and the slope efficiency was increased from 0.37 to 0.53 mW mA^{-1} by inserting a 10 nm thick $Al_{0.75}Ga_{0.25}As$ electron blocking layer. Also, the device became less sensitive to the device temperature, where the amount of increase in the threshold current at an elevated temperature of 95 °C was only 0.27 mA and the slope efficiency dropped by only 24.5%. A peak frequency response of nearly 9 GHz at 5 mA, measured from relative intensity noise (RIN), was obtained in these VCSEL devices.

1. Introduction

VCSEL devices have become the standard in free-space optical communication and local area networks. These surface emission laser devices possess a low divergent angle and circular beam, which lead to simple packaging and low electrical power consumption. The surface emission from the VCSELs also assists the integration of two-dimensional laser array and the facilitation of wafer level testing [1–3]. For VCSEL with 850 nm emission, several methods had been developed to achieve better output performance, including using a strained InGaAsP active region [4–6] and shaping the light-emitting aperture to obtain a high-power single-mode operation [7, 8]. The use of InGaAs or quaternary InAlGaAs quantum wells (QWs) that provided a reasonable compressive strain level had been found to possess a lower threshold current and higher modulation speed [9–12]. It was well known that high output power, low threshold current and especially high temperature stability were the major concerns in semiconductor lasers. While most focus has been put on the enhancements of the reduction in the threshold current, the elevation in modulation frequency response and the high-power operation, the progresses of improving high temperature performance and qualitative analysis in 850 nm VCSELs have been delayed to follow in recent years. The high temperature performance is indubitably related to the amount of current

 © 2006 IOP Publishing Ltd Printed in the UK

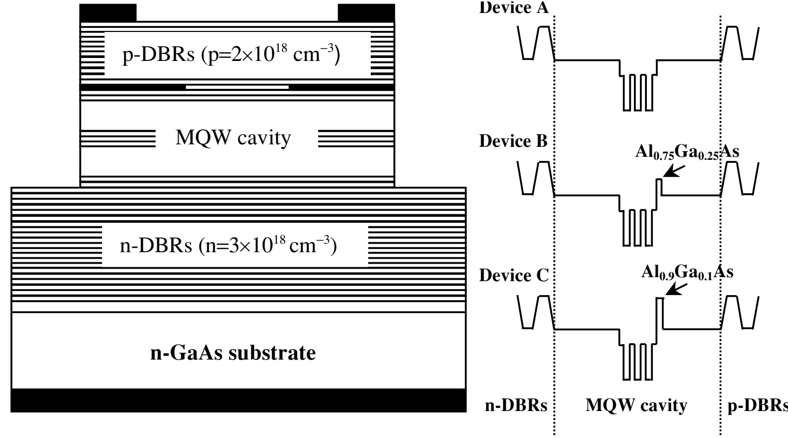

Figure 1. A schematic plot of the VCSEL devices with and without a high-bandgap electron blocking layer.

confined in the active region, which means that the high temperature performance in a laser device can be improved by raising the conduction band offset near the QW active region. Mostly, a thin high-bandgap layer can be grown after the growth of the QW active region to prevent electrons from overflowing out of the QWs [13–15], and hence the carriers can be confined effectively to contribute to stimulated emission. In prior work, we demonstrated 850 nm VCSELs with less temperature sensitivity by inserting a high-bandgap electron blocking layer on the p-side of the InAlGaAs/AlGaAs active region [16]. In this study, the experimental and theoretical analysis of the carrier blocking effect on 850 nm VCSELs was investigated. The simulations were performed by an advanced photonic integrated circuit simulator in three dimensions (PICS3D), which solves the semiconductor and optical wave equations to provide an accurate description of the laser device characteristics. It is a useful tool to access new designs or to optimize existing devices after calibrating with specific materials [17]. VCSELs with carrier blocking layers of 10 nm thick $Al_{0.75}Ga_{0.25}As$ and 13 nm thick $Al_{0.9}Ga_{0.1}As$ were demonstrated and the performances were discussed.

2. The physical model and simulation discussion

A schematic plot of the VCSEL devices with and without a high-bandgap electron blocking layer is shown in figure 1. The devices were assumed to be on the GaAs substrate with a 0.5 μm thick GaAs buffer layer having an n-doping level of 1×10^{18} cm^{-3}. The bottom and top distributed Bragg reflectors (DBRs) consisted of 39 pairs and 21 pairs $Al_{0.15}Ga_{0.85}As/Al_{0.9}Ga_{0.1}As$, which had 99.93% and 99.73% reflectivity, respectively. The active region, which was surrounded by one-wavelength-cavity $Al_{0.6}Ga_{0.4}As$ claddings, was formed by three 7 nm thick $In_{0.15}Al_{0.08}Ga_{0.77}As$ QWs and four 8 nm thick $Al_{0.3}Ga_{0.7}As$ barriers. A 30 nm thick $Al_{0.97}Ga_{0.03}As$ was introduced on the upper cavity spacer layer to form an oxide confinement. A one-wavelength-thick $Al_{0.15}Ga_{0.85}As$ current-spreading layer ($p = 5 \times 10^{18}$ cm^{-3}) and a heavily doped GaAs ($p = 2 \times 10^{19}$ cm^{-3}) contact layer were ultimately put to complete the structure. Three VCSEL devices A, B and C were presented and compared in this study, in which device A was a conventional design, without containing a high-bandgap electron blocking layer on the p-side of the QW active region. Both devices B and C were designed to have an electron blocking layer, in which the material was chosen as AlGaAs with higher Al content because of its natural lattice match to GaAs. The electron blocking layers in devices B and C were 10 nm thick $Al_{0.75}Ga_{0.25}As$ and 13 nm thick $Al_{0.9}Ga_{0.1}As$. For all three devices, the detuning between the QW spontaneous emission and the cavity was 12 nm, where the dip of Fabry–Pérot was 850 nm. The oxide aperture for the three devices was 7 μm in diameter.

The numerical simulation in the present work was executed with the use of the PICS3D program, which could be used to access the optimization of the existing devices by calibration of a specific material. In this program, the valence-band structure, which included the coupling of the heavy-hole (HH), the light-hole (LH) and the spin–orbit split-off bands, was calculated by a 6×6 Hamiltonian with envelop function approximation [18]. The optical gain spectra with the valence-band-mixing effect could be expressed as [19]

$$g(E) = \frac{g_0}{2\pi t E} \sum_{i,j} \int_0^\infty \frac{(\pi/\Gamma) f_{\mathrm{dip}}(k_t) M_b (f_j - f_i)\, \mathrm{d}k_t^2}{1 + (E_{cj}(k_t) - E_{kpi}(k_t) - E)^2/\Gamma^2}, \quad (1)$$

where t is the thickness of the QW and $\Gamma = \hbar/\tau_{\mathrm{scat}}$ is the broadening due to intraband scattering relaxation time τ_{scat}. E_{cj} is the jth conduction subband and E_{kpi} is the ith valence subband from the $k \cdot p$ calculation. The sum is over all possible conduction and valence subbands. $g_0 = \pi q^2 \hbar / \varepsilon_0 c m_0^2 n$ is a constant with all symbols having their usual meanings. M_b is a dipole moment.

The illustration of electrical behaviour of a VCSEL in this study was governed by Poisson's equation:

$$-\nabla \cdot \left(\frac{\varepsilon_0 \varepsilon_{dc}}{q} \nabla V \right) = -n + p + N_D(1 - f_D) - N_A f_A + \sum_j N_{tj}(\delta_j - f_{tj}). \quad (2)$$

The current continuity equations for electrons and holes were

$$\nabla \cdot J_n - \sum_j R_n^{tj} - R_{\mathrm{sp}} - R_{\mathrm{st}} - R_{\mathrm{au}} + G_{\mathrm{opt}}(t) = \frac{\partial n}{\partial t} + N_{\mathrm{D}} \frac{\partial f_{\mathrm{D}}}{\partial t}, \quad (3)$$

Table 1. Parameters of AlAs, GaAs and InAs used in the calculation.

Parameter	Symbol (unit)	AlAs	GaAs	InAs
Luttinger parameters	γ_1	3.76	6.98	20.0
	γ_2	0.82	2.06	8.5
	γ_3	1.42	2.93	9.2
Varshni parameters	α (meV K^{-1})	0.885	0.5045	0.276
	β (K)	530	204	93
	$E_g(T=0)$ (eV)	3.099	1.519	0.417
Elastic stiffness constants	C_{11} (10^{11} dyn cm^{-2})	12.50	12.21	8.329
	C_{12} (10^{11} dyn cm^{-2})	5.34	5.66	4.526
Hydrostatic deformation potential	a (eV)	−8.11	−8.33	−6.08
Shear deformation potential	b (eV)	−2.3	−2.0	−1.8
Effective mass of electrons	m_e/m_o	0.15	0.067	0.026
Spin–orbit split-off energy	Δ (eV)	0.28	0.341	0.39
Lattice constant	a_0 (Å)	5.6611	5.653 25	6.0583

$$\nabla \cdot J_p + \sum_j R_p^{tj} + R_{\rm sp} + R_{\rm st} + R_{\rm au} - G_{\rm opt}(t) = -\frac{\partial p}{\partial t} + N_{\rm A}\frac{\partial f_{\rm A}}{\partial t}, \quad (4)$$

where V is the electrostatic potential and n and p are the electron and hole concentrations. J_n and J_p denote the carrier flux density. N is the doping impurity where the subscripts D and A are used to denote donor and acceptor, respectively. R represents the recombination rate and G is the generation term. The electron and hole concentrations were defined by Fermi–Dirac distribution and a parabolic density of state. For QWs, the following equations were given to express the density of electrons and holes in a QW:

$$n = \sum_j \rho_j^0 kT \ln[1 + {\rm e}^{(E_{fn}-E_j)/kT}] + \text{unconfined electrons}, \quad (5)$$

$$p = \sum_i \rho_i^0 kT \ln[1 + {\rm e}^{(E_i-E_{fp})/kT}] + \text{unconfined holes}, \quad (6)$$

where the subscript i denotes all confined states for different hole bands and j denotes those for the Γ and L bands. The number of unconfined carriers was calculated using Fermi–Dirac statistics. For current transport across the junctions, the thermionic emission theory [20], defined by

$$J_{\rm hn} = \gamma_{\rm hn} \cdot \bar{v}_{\rm bn}^{\rm therm} \cdot (n_{\rm b} - n_{\rm b0}), \quad (7)$$

$$J_{\rm hp} = \gamma_{\rm hp} \cdot \bar{v}_{\rm bp}^{\rm therm} \cdot (p_{\rm b} - p_{\rm b0}), \quad (8)$$

is used, where $\gamma_{\rm hn}$ and $\gamma_{\rm hp}$ are the correction constants, $\bar{v}$ is the thermal recombination velocity, $n_{\rm b}$ and $p_{\rm b}$ denote the electron and hole concentrations on the barrier side of the junction and $n_{\rm b0}$ and $p_{\rm b0}$ are the corresponding concentrations when the quasi-Fermi levels are the same as those on the opposite side. These equations ensure that the net current is zero when the quasi-Fermi levels on both sides of the barriers are the same. The quantum tunnelling effect is only taken into account when solving the carrier transport in the multiple-quantum-well active region; however, it is neglected when solving the carrier transport in the bulk region, including the electron blocking layer.

The material parameters of the binary semiconductors could be found in table 1. The unstrained InAlGaAs bandgap energies could be expressed as a weighted sum of the bandgap energies of relevant ternary semiconductors with appropriate bandgap bowing parameters. Specifically, the unstrained InAlGaAs bandgap energies were calculated by following expressions [21]:

$$E_g(\text{InGaAlAs}) = \frac{xyE_g^u(\text{GaAlAs}) + yzE_g^v(\text{InAlAs}) + xzE_g^w(\text{InGaAs})}{xy + yz + zx}, \quad (9)$$

$$E_g^u(\text{GaAlAs}) = uE_g(\text{AlAs}) + (1-u)E_g(\text{GaAs}) - u(1-u)B(\text{GaAlAs}), \quad (10)$$

$$E_g^v(\text{InAlAs}) = vE_g(\text{InAs}) + (1-v)E_g(\text{AlAs}) - v(1-v)B(\text{InAlAs}), \quad (11)$$

$$E_g^w(\text{InGaAs}) = wE_g(\text{InAs}) + (1-w)E_g(\text{GaAs}) - w(1-w)B(\text{InGaAs}), \quad (12)$$

$$u = \frac{1-x+y}{2}, \quad v = \frac{1-y+z}{2}, \quad w = \frac{1-x+z}{2}, \quad (13)$$

where x, y and $z = 1 - x - y$ represent the compositions of Ga, Al and In in the InAlGaAs material system, respectively. The bandgap bowing parameters of AlGaAs, InAlAs and InGaAs were $0.127 + 1.310y$, 0.70 and 0.477 eV, respectively. The temperature-dependent bandgap energies of the binary semiconductors were calculated using the Varshni formula [22]. The conduction band offset for the compressively strained InAlGaAs/AlGaAs QW was assumed to be 67% of the total band offset [23]. For the treatment of device heating, the thermoelectric power and the thermal current induced by temperature gradient are solved utilizing the method provided by Wachutka [24]. Various heat sources, including Joule heat, generation/recombination heat, Thomson heat and Peltier heat, are taken into account in this specific study. During the simulations, the VCSEL devices were built up layer by layer except for the stepped $Al_{0.15}Ga_{0.85}As/Al_{0.9}Ga_{0.1}As$ DBRs which were assumed to be a bulk layer having an averaged Al content with the same thickness under simulation efficiency concern. It was convenient and might not influence the qualitative simulation results in this study because we

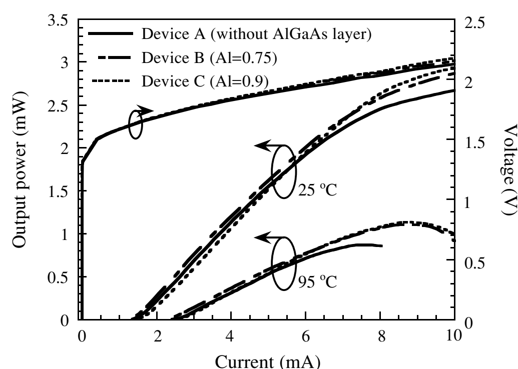

Figure 2. Simulation results of the RT light output and voltage versus current characteristics of devices A, B and C. The electron blocking layers for devices B and C are 10 nm thick $Al_{0.75}Ga_{0.25}As$ and 13 nm thick $Al_{0.9}Ga_{0.1}As$, respectively.

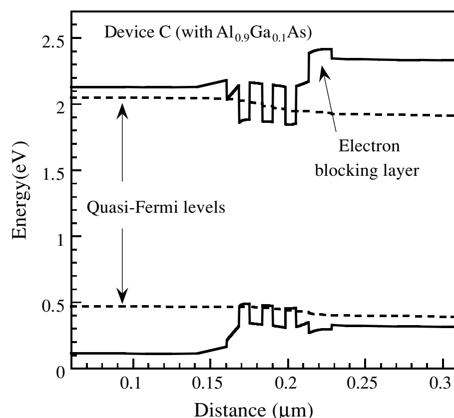

Figure 3. Expanded energy band diagram near the QW active region of device C. The diagram was obtained at RT with an applied voltage of 2.1 V.

specifically focused on the carrier blocking effect on the VCSEL devices by employing a high-bandgap layer on the p-side of the QW active region.

The room temperature (RT) light output and voltage versus current (L–I–V) characteristics of the devices A, B and C studied in simulation are shown in figure 2. It was found theoretically that the threshold current was slightly reduced and the laser output power at the high current injection region was enhanced by inserting a 10 nm thick $Al_{0.75}Ga_{0.25}As$ electron blocking layer in device B. However, when the electron blocking layer was substituted to be a thicker (13 nm) and higher Al content $Al_{0.9}Ga_{0.1}As$ layer, the threshold current in device C was increased in the opposite way. Nevertheless, the slope efficiency and the maximum output power at roll over point in device C were improved. The decreased threshold current in device B should be attributed to the increase of optical confinement factor value, and hence enhancing the radiative and stimulated recombination in the QWs. The values of optical confinement factor for devices A, B and C were 2.812%, 2.853% and 2.869%, respectively. For device C, even the value of optical confinement factor was the highest among the three devices, the holes in the valence band would meet a higher and thicker barrier when injecting into QWs because of the higher Al content and the thicker electron blocking layer.

To further explain the difficulty of hole injection into QWs when using a 13 nm thick $Al_{0.9}Ga_{0.1}As$ as an electron blocking layer in device C, the expanded energy band diagram near the QW active region is shown in figure 3. The diagram was obtained at RT with an applied voltage of 2.1 V (10 mA). The left-hand side of the diagram shows the n-side of the VCSEL device, and the dashed lines represent the quasi-Fermi levels. It was shown that the high-bandgap $Al_{0.9}Ga_{0.1}As$ layer was on the p-side of the QW active region. And, because the electrons have higher mobility than the holes, the $Al_{0.9}Ga_{0.1}As$ layer can act as an electron blocking layer to prevent electron leakage and hence improve the laser performance at high current injection. However, the increased barrier height in the valence band would result in the difficulty of hole injection into QWs when the device was at lower current injection and therefore increasing the threshold current.

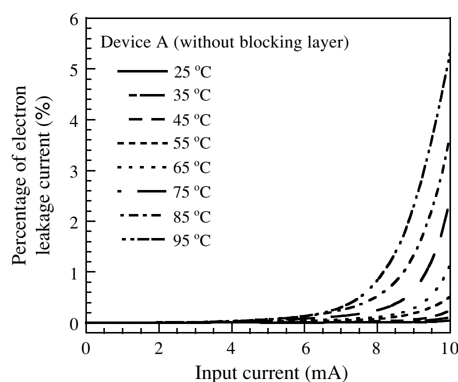

Figure 4. Percentage of the electron leakage current as a function of the input current in device A when the device temperature was in the range of 25–95 °C.

Next, the electron leakage current as a function of the input current and the device temperature was discussed. In this study, the percentage of the electron leakage current was defined as the ratio of the current overflowed to the p-type layer to that injected into the devices. As an example of device A, the percentage of the electron leakage current as a function of the input current when the device temperature was in a range of 25–95 °C is indicated in figure 4. Higher percentage of the electron leakage current was found when the input current was increased, and the percentage of the electron leakage current increased rapidly when the device temperature increased. It is reasonable because the electrons will have higher kinetic energy and the probability of electrons overflowing away from the QWs is increased when the device temperature increases. The percentage of the electron leakage current as a function of the device temperature for devices A, B and C is shown in figure 5. The total input current for all three devices was 10 mA and the device temperature under discussion was in a range of 25–95 °C. We found that the percentage of the electron leakage current could be apparently reduced using a high-bandgap AlGaAs layer. Therefore, as depicted from the simulation results, the laser output performance of a 850 nm VCSEL can be improved by inserting a high-bandgap electron blocking layer to reduce the electron leakage current.

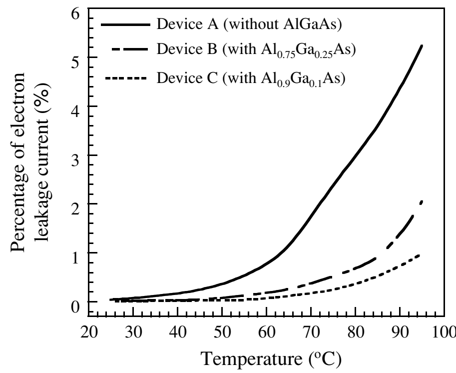

Figure 5. Percentage of the electron leakage current as a function of the device temperature for devices A, B and C. The curves were obtained when the devices were biased at 10 mA.

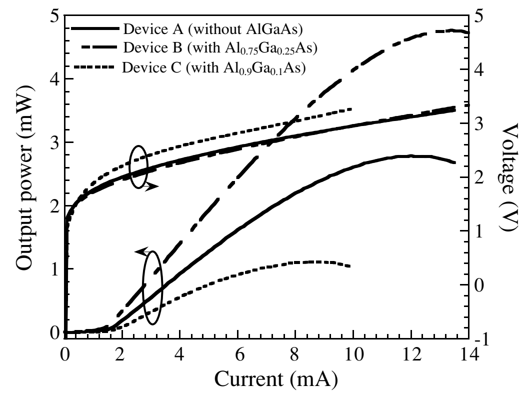

Figure 6. RT L–I–V characteristic of the fabricated VCSELs for devices A, B and C with an oxide aperture of 7 μm.

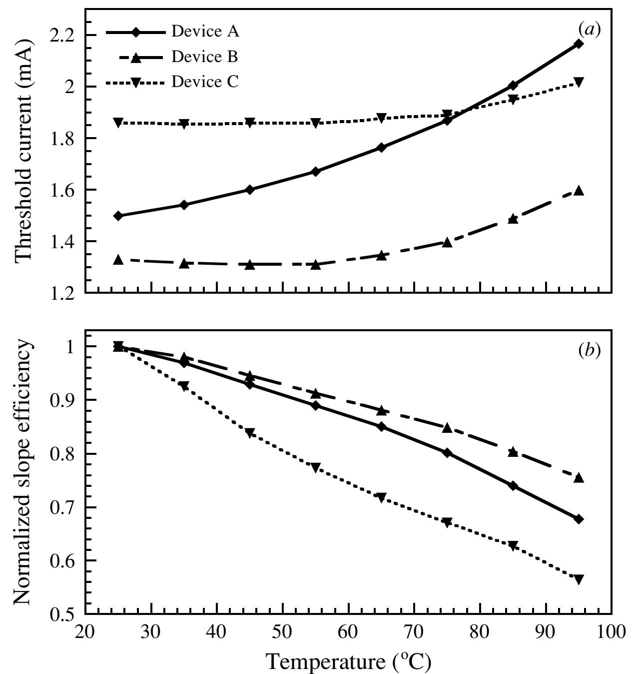

Figure 7. Experimental temperature-dependent variation of the threshold current and slope efficiency of devices A, B and C.

Especially, a 10 nm thick $Al_{0.75}Ga_{0.25}As$ may be appropriate because of the reduced threshold current and better laser output performance under high temperature operation.

3. Device fabrication and characteristics

After numerically investigating the carrier blocking effect on 850 nm VCSELs, we tried to fabricate the devices experimentally in accordance with the simulations. All the three devices A, B and C were prepared on n-type GaAs (1 0 0) substrates by low pressure (50 Torr) metal-organic chemical vapour deposition (MOCVD) with group-V precursor of arsine (AsH_3). Trimethyl (TM) sources of aluminium (Al), gallium (Ga) and indium (In) were used for group-III precursors. The dopant sources for n and p types were SiH_4 and CBr_4. Epitaxial device structures were all consistent with the designs in simulation. The growth rate, compositions and doping concentrations in each layer were carefully determined by a series of samples. The growth temperature of the n-type DBRs and the active region was 720 °C and that of the p-type DBRs was 670 °C. The detuning between the photoluminescence (PL) emission and the cavity was also aligned to 12 nm. After epitaxy, the fabrication process began from depositing a 1.3 μm thick SiN_x layer, which acted as a hard mask in the following process, onto the wafer by plasma-enhanced chemical vapour deposition (PECVD) at 300 °C. Standard photolithography and reactive ion etching (RIE) using SF_6 with a flow rate of 20 sccm as etching gas were then performed to define etching pattern on the hard mask. Trench mesa etching by Cl_2 with a flow rate of 2 sccm and Ar plasma were performed to transfer the mask pattern onto the wafer. The etching depth was cautiously controlled to penetrate the active region, and the 30 nm thick $Al_{0.97}Ga_{0.03}As$ aperture layer was exposed for selective oxidation in 400 °C stream environment. After oxidation, the residual dielectric was removed and a second 150 nm thick SiO_2 by PECVD was deposited for passivation, followed by a partially etched process for contact window. Ti (30 nm)/Pt (50 nm)/Au (200 nm) were deposited onto the heavily p-doped GaAs contact layer for p-contact, and AuGe (50 nm)/Ni (20 nm)/Au (350 nm) were deposited for n-contact.

For each design of the fabricated VCSELs, nine devices were randomly selected to measure the output characteristics, and the discrepancy of the nine devices for each design was negligibly small. Figure 6 shows the RT L–I–V characteristic of the fabricated VCSELs for devices A, B and C. The oxide aperture for all the three devices was 7 μm in diameter and was determined from a series of calibration samples having similar structure design. In device A, a threshold current of 1.47 mA with a slope efficiency of 0.37 mW mA^{-1} and a threshold voltage of 1.85 V were obtained. The L–I curve started to roll over at about 2.8 mW as a result of internal heating effect. In device B, the laser output performance was found to be improved by inserting a 10 nm thick high-bandgap $Al_{0.75}Ga_{0.25}As$ electron blocking layer, as indicated in the simulations. The threshold current of device B was reduced to 1.33 mA with a slope efficiency of 0.53 mW mA^{-1}, while a maximum power of 4.7 mW was achieved. However, it was found in device C that the threshold current increased to 1.87 mA and the slope efficiency became 0.26 mW mA^{-1} when a 13 nm thick $Al_{0.9}Ga_{0.1}As$ layer was substituted as

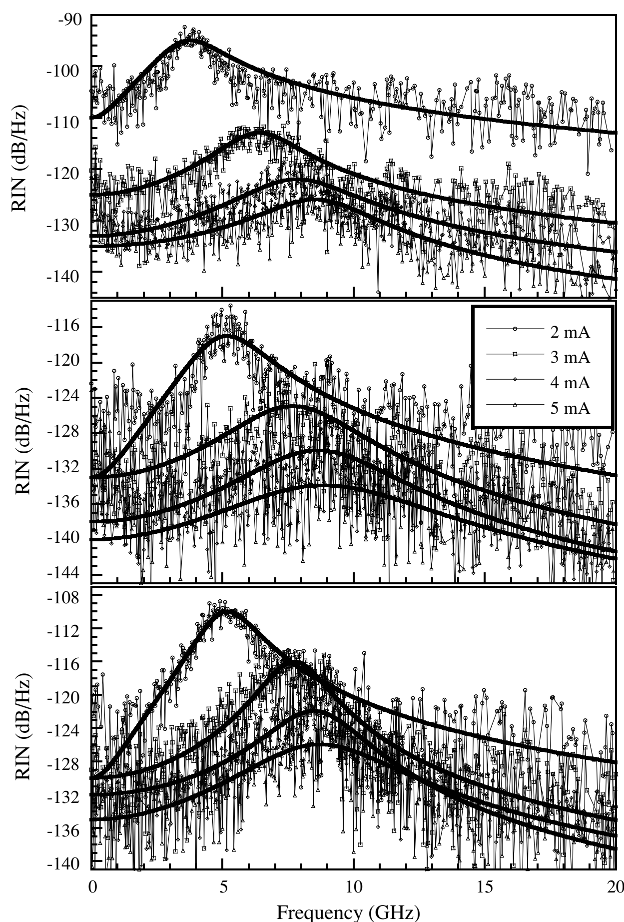

Figure 8. RT relative intensity noise (RIN) value of the three devices in the bias current range of 2–5 mA.

the high-bandgap electron blocking layer. The decreased output performance might be attributed to the higher resistance during the device process and the small distance between the $Al_{0.9}Ga_{0.1}As$ electron blocking layer and the QWs that degraded the crystal quality during the oxidation process. The increase of the threshold current in device C might also be partially due to the difficulty of hole injection into QWs from numerical simulation analysis. The discrepancy of the slope efficiencies between theory and experiment may be attributed to the fact that the thermal behaviour of a VCSEL is difficult to characterize in theoretical calculation.

Figure 7 shows the experimental temperature-dependent variation of the threshold current and slope efficiency of devices A, B and C. As compared with the standard design of device A, device B showed a less temperature-sensitive output performance, where the amount of increase in the threshold current at an elevated temperature of 95 °C was only 0.27 mA and the slope efficiency dropped by only 24.5%. The threshold current of device A increased to 2.17 mA with a slope efficiency reduction of 32% when the substrate temperature was 95 °C. For device C, the increase of the threshold current was from 1.85 to 2.01 mA with a slope efficiency reduction of 43% when the substrate temperature increased from 25 to 95 °C.

The measured RIN value of the devices is shown in figure 8, where the solid lines are the fitting curves in accordance with the RIN transfer function:

$$\mathrm{RIN} = \frac{4}{\pi}\delta f_{\mathrm{st}} \frac{f^2 + (\gamma/2\pi)^2}{\left(f_r^2 - f^2\right)^2 + f^2(\gamma/2\pi)^2}, \quad (14)$$

where f_r represents the resonant frequency and r is the damping rate. The RIN illustrated the maximum available amplitude range for signal modulation and served as a quality indicator of a laser. The value of RIN could be thought as a type of inverse carrier-to-noise ratio measurement and could be defined as the ratio of the mean-square optical intensity noise to the square of the average optical power. The RIN values of the three devices were obtained in a bias current range of 2–5 mA. As the bias current increased, the peak RIN frequency responses of the three devices increased respectively, and a frequency response of 8.5 GHz for device A, 8.9 GHz for device B and 8.7 GHz for device C was obtained when the bias current was 5 mA. The results also suggest that the insertion of an electron blocking layer to reduce the electronic leakage current and improve the light output performance does not deteriorate the frequency response.

4. Conclusion

In summary, we had theoretically and experimentally investigated the carrier blocking effect on the output performance of 850 nm InAlGaAs/AlGaAs VCSELs. The results obtained theoretically indicated that the output performance could be enhanced by inserting a carrier blocking layer on top of the QW active region to reduce the electron leakage current. The VCSELs with and without a carrier blocking layer were also fabricated experimentally. It was found that a 10 nm thick $Al_{0.75}Ga_{0.25}As$ should be the better candidate for the electron blocking layer because of the reduced threshold current, higher slope efficiency and better stable laser output performance under high temperature operation.

Acknowledgments

The authors would like to thank the Industrial Technology Research Institute in Taiwan for technical support. This work was supported by the National Science Council, Republic of China, under grants NSC94-2752-E-009-007-PAE, NSC94-2120-M-009-007 and NSC94-2112-M-018-009.

References

[1] Wilmsen C W, Temkin H and Coldren L A 1999 *Vertical-Cavity Surface-Emitting Lasers: Design, Fabrication, Characterization, and Applications* (Cambridge: Cambridge University Press)

[2] Peters F H and MacDougal M H 2001 *IEEE Photonics Technol. Lett.* **13** 645

[3] Gilor J, Samid I and Fekete D 2004 *IEEE J. Quantum Electron.* **40** 1355

[4] Sale T E, Amano C, Ohiso Y and Kurokawa T 1997 *Appl. Phys. Lett.* **71** 1002

[5] Tansu N, Zhou D and Mawst L J 2000 *IEEE Photonics Technol. Lett.* **12** 603

[6] Chang Y-S, Kuo H-C, Lai F-I, Chang Y-A, Lu C-Y, Laih L-W and Wang S-C 2004 *J. Lightwave Technol.* **22** 2828

[7] Shi J-W, Yen J-L, Jiang C-H, Chen K-M, Hung T-J and Yang Y-J 2006 *IEEE Photonics Technol. Lett.* **18** 481
[8] Shi J-W, Jiang C-H, Chen K-M, Yen J-L and Yang Y-J 2005 *Appl. Phys. Lett* **87** 031109
[9] Ko J, Hegblom E R, Akulova Y, Thibeault B J and Coldren L A 1997 *IEEE Photonics Technol. Lett.* **9** 863
[10] Choi H-K and Wang C-A 1990 *Appl. Phys. Lett.* **57** 321
[11] Chen T-R, Zhao B, Eng L, Zhoung Y-H, O'Brien J and Yariv A 1993 *Electron Lett.* **29** 1525
[12] Choi H-K, Wang C-A, Kolesar D F, Aggrawal R L and Walpole J N 1991 *IEEE Photonics Technol. Lett.* **3** 857
[13] Stringfellow G B and Craford M G 1997 *High Brightness Light Emitting Diodes* (San Diego: Academic)
[14] Hansen M, Piprek J, Pattison P M, Speck J S, Nakamura S and DenBaars S P 2002 *Appl. Phys. Lett.* **81** 4275
[15] Onischenko A I, Sale T E, O'Reilly E P, Adams A R, Pinches S M, Frost J E F and Woodhead J 2000 *IEE Proc. Optoelectron.* **147** 15
[16] Chang Y-A, Lai F-I, Yu H-C, Kuo H-C, Laih L-W, Yu C-Y and Wang S-C 2005 *Japan. J. Appl. Phys.* **44** L901
[17] *PICS-3D* Crosslight Inc. Software, Canada (http://www.crosslight.ca)
[18] Chang C-S and Chuang S-L 1995 *IEEE J. Sel. Top. Quantum Electron.* **1** 218
[19] Chuang S-L 1995 *Physics of Optoelectronic Devices* (New York: Wiley)
[20] Sze S M 1981 *Physics of Semiconductor Devices* 2nd edn (New York: Wiley) p 255
[21] Adachi S 1987 *J. Appl. Phys.* **61** 4869
[22] Vurgaftman I, Meyer J R and Ram-Mohan L R 2001 *J. Appl. Phys.* **89** 5815
[23] Jensen J R, Hvam J M and Langbein W 1999 *J. Appl. Phys.* **86** 2584
[24] Wachutka G K 1990 *IEEE Trans. Comput.-Aided Des. Integr. Circuits Syst.* **9** 1141